Available online at www.sciencedirect.com

ScienceDirect

Geochimica et Cosmochimica Acta 121 (2013) 1–14

Geochimica et Cosmochimica Acta

www.elsevier.com/locate/gca

Identification by Raman spectroscopy of Mg–Fe content of olivine samples after impact at 6 km s^{-1} onto aluminium foil and aerogel: In the laboratory and in Wild-2 cometary samples ☆

N.F. Foster [a], P.J. Wozniakiewicz [a], M.C. Price [a], A.T. Kearsley [b], M.J. Burchell [a,*]

[a] Centre for Astrophysics and Planetary Science, School of Physical Sciences, Univ. of Kent, Canterbury, Kent CT2 7NH, UK
[b] Department of Mineralogy, The Natural History Museum, London SW7 5BD, UK

Received 2 November 2012; accepted in revised form 17 July 2013; Available online 26 July 2013

Abstract

Olivine, $(Mg, Fe)_2[SiO_4]$, is a common mineral in extraterrestrial materials, whose Mg–Fe content varies from the end-members Forsterite (Mg_2SiO_4: denoted 'Fo') to Fayalite (Fe_2SiO_4: denoted 'Fa'), together with minor quantities of Ca, Cr, Mn and Ni. Olivine is readily identified by Raman spectroscopy, and the Mg–Fe content can be obtained by precise measurements of the position of the two strongest Raman peaks. Here we show that this is not only true for pristine and highly crystalline olivine, but also for grains which have undergone high pressure shock processing during hypervelocity impact. We demonstrate that there are subtle changes to the Raman spectra in grains impacted at 6.1 km s^{-1} onto aluminium foil and into low density aerogel. We quantify these changes, and also show that if no correction is made for the impact effects, the Fe:Mg molar ratio of the olivine can be significantly misinterpreted. This study was stimulated by NASA's *Stardust* mission to comet 81P/Wild-2, since freshly ejected cometary dust particles were collected (via impact) onto aluminium foil and into aerogel cells at 6.1 km s^{-1} and these samples are being investigated with Raman spectroscopy. We identify the residue in one *Stardust* impact crater on aluminium foil as arising from an olivine with a composition of $Fo_{97–100}$.

1. INTRODUCTION

Olivine is an abundant mineral in our Solar System, with parageneses spanning from nebular processes before planetesimal accretion to the present-day differentiation of igneous melts on planetary bodies. As well as being a major component of meteoritic and cometary materials (e.g. Zolensky et al., 2008), it also been observed in dust clouds around various stars (see Henning, 2010 for a recent review). Its formula, $(Mg,Fe)_2[SiO_4]$, indicates that the Mg and Fe content is variable, and the complete range of these variants is found in nature, along with minor substitutions of other divalent metal cations. The Mg rich end-member of the family is Forsterite (denoted here as 'Fo_{100}'), whilst the Fe rich end member is Fayalite (Fo_{00}) where the subscript indicates the Fe:Mg molar ratio, Mg/(Mg + Fe). Olivine gives strong Raman scattering, producing two distinctive peaks with Raman shifts of typically 820 (referred to as the '*P*1' line) and 850 cm^{-1} (the '*P*2' line) which arise from a mixture of symmetric and anti-symmetric internal stretching vibrational modes of the SiO_4 ions (Chopelas, 1991). The two peak structure persists to pressures of up to 50 GPa (Durden et al., 1993). The peak amplitude ratio of *P*1 and *P*2 in individual spectra may reflect the crystallographic orientation of the grains being analysed. It has previously been shown (Kuebler et al., 2006) that by accurately measuring the wave-number positions of these two peaks, it is possible to extract the molar Mg:Fe ratio of an olivine to within 10 Fo units. How this correlation of the Raman

* Corresponding author. Tel.: +44 (0)1228 823248.
E-mail address: m.j.burchell@kent.ac.uk (M.J. Burchell).

0016-7037/$ - see front matter © 2013 The Authors. Published by Elsevier Ltd. All rights reserved.
http://dx.doi.org/10.1016/j.gca.2013.07.022

spectra with the Fo molar content arises is discussed in detail in Kuebler et al. (2006), but briefly the difference in the atomic masses and the associated bond strengths, means that as Mg and Fe substitute for each other, the Si–O vibrational frequencies are altered and hence so are the positions of the main Raman peaks. So far, there has been little investigation of the role of other elements (e.g. Cr and Mn) in modifying Raman spectra.

The recent NASA *Stardust* mission to comet 81P/Wild-2 captured dust, freshly emitted from the comet, during a fly-by at 6.1 km s^{-1} (Brownlee et al., 2006). It captured the cometary dust by deploying a collector containing SiO_2 aerogel cells and aluminium foils (Tsou et al., 2003). Aerogel has now long been used in space to collect dust in high speed impacts (see Burchell et al., 2006a for a review). It is highly porous, so has a very low density. For example, the SiO_2 aerogel used on *Stardust* had a graded density profile, designed to be 5 mg/cc at the front face rising to 50 mg/cc at the rear of the aerogel blocks (which were 3 cm deep). In aerogel, a fast moving particle tunnels in and deposits material along the walls of, and at the end of, the resultant track. The track itself is visible (SiO_2 aerogel is mostly transparent) and can be studied optically as detailed in Burchell et al. (2008a) who report on the optical measurement of the first 180 cometary dust tracks observed in the *Stardust* aerogel. Based on comparison with laboratory experiments, Burchell et al. (2009a) estimated that the *Stardust* aerogel behaved as if it had an overall bulk density of ~20 mg/cc. Given impacts at 6.1 km s^{-1} onto aerogel of 20 mg/cc, it is estimated (Trigo-Rodríguez et al., 2008) that the peak shock pressure experienced by the impacting particle will have been approximately 800 MPa.

Several authors have estimated the temperatures small particles experience on their surfaces during capture in aerogel. For example, Burchell et al. (2009a) observe melting and ablation of stainless steel projectiles during capture in aerogel, and hence estimate sustained temperatures in excess of 1400 °C. Hörz et al. (2009) similarly observed surface melting on Al_2O_3 spheres captured in aerogel and estimate particle surface temperatures in excess of 2054 °C. The duration of such heating (as well as its magnitude) is of importance, and we note that Noguchi et al. (2007) report mineralogical changes in samples captured in aerogel in the laboratory, indicating that temperatures in excess of 500 °C were maintained for timescales of at least a few microseconds. Given these shock pressures and elevated temperatures, it is possible that capture effects will alter the apparent mineralogy of grains captured in aerogel.

The *Stardust* collector also carried aluminium foils (Al-1100, 103 μm thick) and when small cometary dust grains struck these foils they left classic bowl-shaped impact craters, or shallow craters with multiple pits, lined with melted residue. This is typical of these hypervelocity impacts. Burchell and Kearsley (2009) estimated that a typical olivine grain impacting one of these foils would have experienced a peak shock pressure of approximately 85–90 GPa, whilst Wozniakiewicz et al. (2012a) calculated that Mg-rich olivine would experience a peak pressure of 79 GPa. Given that the particle fragments during impact, and that much of the projectile material is melted, it is likely that the mineralogical characteristics determined after capture will not be the same as those of the raw, pre-impact, grain.

Accordingly, in preparation for the return of the *Stardust* samples, many analysis techniques were carried out on samples fired in the laboratory using two-stage light gas guns into aerogel and onto aluminium foils. Such guns can readily achieve speeds of 6.1 km s^{-1} so are ideal for this purpose. Indeed, it was in this way, that Burchell et al. (2001) demonstrated that Raman spectroscopy could be performed in situ on grains captured in aerogel, and obtained recognisable spectra. In their paper, the authors used olivine and enstatite as the samples, although they presented no detailed mineralogical information (e.g. precise Mg:Fe ratio) beyond identification of the mineral species. The same group later showed that some organic particles could also provide Raman spectra after capture in hypervelocity impacts (Burchell et al., 2004). They subsequently reported on a wider range of mineral and meteoritic materials captured in aerogel in the laboratory and subsequently identified by Raman spectroscopy, including mapping the location of the carbon content of a captured dust grain (Burchell et al., 2006b). Perhaps more surprisingly, they also showed that even the impact residues (often assumed to be entirely melted) lining craters after impacts on aluminium foil at 6 km s^{-1}, could yield Raman spectra from the original projectiles, i.e. had retained a degree of their original crystalline structure (Burchell et al., 2008b).

There is thus a wide body of evidence showing that Raman techniques can be applied to dust grains captured in high speed impacts on foils and into aerogel. There are caveats however: not all minerals tested after impacts onto aluminium foil in Burchell et al., (2008b) showed Raman spectra; for example, lizardite (a phyllosilicate) gave no recognizable Raman spectra after capture, and tests on organic particles captured in aerogel showed that surface processing of the grains was very speed dependent. For example, for some impacted organics the distinct Raman spectra that could be seen after aerogel capture at 1 km s^{-1}, were no longer visible in impacts at 6 km s^{-1} (Burchell et al., 2009b). Additionally, where organic-rich particles captured in aerogel at 6 km s^{-1} were studied using the D and G carbon bands, it was found by Fries et al. (2009), that the G band signal showed changes after capture. Note that the G band was used as a better indicator of changes than the D band, as the D band is widely considered not to be a "pure" Raman band as it is known to change position depending on the illuminating laser frequency. The results of Fries et al. (who used various coal particles as projectiles) suggest that amorphisation and recrystallisation may have occurred in varying degrees within their organic samples.

Indeed, given that capture, even in aerogel, involves high shock pressures and elevated temperatures, it should be no surprise that mineralogical changes, or processing of organics, occur in captured particles, especially at their surface which is where the Raman signals are generated. Therefore studies of dust grains captured in space (such as that of the organic content of grains presented in Sandford et al. (2006) or Rotundi et al. (2008)) need to be seen in the light of studies such as that of Fries et al. (2009) which use laboratory

analogues to investigate capture effects that may bias the interpretation of results from natural samples.

A Raman study of two cometary dust grains captured in aerogel by *Stardust* has already been published (Bridges et al., 2010). That work found an iron-oxide composition to the grains, and featured careful laboratory analogue studies to determine if the observed magnetite and hematite were indigenous to the dust grains pre-capture, or could have arisen as a result of processing during the capture event in the aerogel. A separate study of other Stardust cometary dust grains captured in aerogel by Wopenka (2012), also found evidence for pyrrhotite and olivine. In the latter case, by comparison with Raman spectra from standards, the olivine was identified as $Fa_{30}Fo_{70}$, but no correction was applied for any capture-associated alteration.

Herein we present the results of a study of the effects of high speed capture in aerogel and onto aluminium foil of a suite of olivines (of differing Mg–Fe content). We then compare our results with an analysis of two cometary *Stardust* grains: one captured in aerogel and another which impacted aluminium foil.

2. METHOD

The olivine powders used for the laboratory studies in this work were taken from the suite already reported in Wozniakiewicz et al. (2009). These synthetic olivines form a series Fo_{00}, Fo_{20}, Fo_{40}, Fo_{60}, Fo_{80} and Fo_{100}. In the earlier work, analytical scanning electron microscopy using energy dispersive X-ray microanalysis (SEM-EDX) showed that the majority had a well constrained homogeneous composition, but some samples contained a broader range of compositions (see Table 1, where the mean values plus minimum and maximum observed values are given). There was little, if any, variation of Mg:Fe ratio within each of the $Fo_{40,\ 80\ and\ 100}$ samples. However, the SEM-EDX work showed that grains of the Fo_{20} and Fo_{60} samples had a range of different Fo compositions, with the Fo_{20} sample varying from $Fo_{17–26}$ whilst the Fo_{60} sample varied between $Fo_{48\text{-}72}$. In addition, whilst the Fo_{00} sample showed little if any Mg content, the SEM study showed areas of FeO and SiO_2. Therefore in some of the Raman studies here the data show a scatter which reflects this underlying range of Fo contents.

In general, the grains in each sample were porous, irregular in shape and polydispersive, of >300 μm size. However, the wide range of impact features shows that many projectiles broke up during handling and firing in the gun, resulting in a spray of smaller fragments striking the targets. In addition, for the impacts on aerogel, a powdered sample of natural San Carlos olivine was also used (a gemstone peridot from Arizona, USA). This olivine has previously been well characterised, and is known to have a very narrow range of composition close to Fo_{92}.

The Raman analysis of samples was carried out using a HeNe laser (632.8 nm), a Jobin-Yovin SA HR640 spectrometer (cooled with liquid nitrogen), and an Olympus BX40 microscope. The spectrometer had a CCD with 1024 × 256 pixels and a 1200 lines/mm grating. Beam sizes on the target where of the order of a few micrometres. This was the same Raman instrument used in previous work by Burchell et al. (2001, 2004, 2006b, 2008b, 2009b) involving identification of mineral and organic samples after hypervelocity impacts. During analysis of the samples, the Raman spectra were obtained with LabSpec (version 3.03) software and then processed using Galactic GRAMS/32 AI peak-fitting software, where individual peaks were fitted with a Gaussian–Lorentzian shape. The accuracy of the system was controlled by repeated use of a silicon wafer calibration standard exhibiting the well-known, narrow peak at 520.6 cm^{-1}.

Table 1
Olivine sample Fo contents and the impact speeds in laboratory shots at aluminium foil and aerogel (a null entry "–" implies no spread observed in Fo content).

Sample name	Minimum	Fo range	Max	Impact speed (km s^{-1})	
		Mean		Foil	Aerogel
Fo_{00}	–	0	–	6.08	–
Fo_{20}	17	20	26	5.93	–
Fo_{40}	38	40	41	6.01	6.1
Fo_{60}	48	60	72	6.08	–
Fo_{80}	77	79	81	6.01	6.1
Fo_{100}	–	100	–	6.08	6.1

The targets were impacted by projectiles fired in a two-stage light gas gun at the University of Kent (Burchell et al., 1999). This fires a nylon discarding-sabot, which is filled with milligrams of the projectile material. The speed of the shot is chosen in advance and is controlled by varying the gas pressure in the pump-tube and the amount and type of the gunpowder used (see Burchell et al., 1999 for details). The speed is then measured in each shot by sensors along the range of the gun which detect time of exit from the launch tube, impact of the sabot on a plate part way along the range, and impact on the target. These timings give speed measurement with an accuracy of ±4% when used with small projectile grains. Speeds can be measured to higher precision by passage of larger projectiles through light curtains positioned along the range of the gun, but this is not so effective when using small projectiles, as in the present work.

Two suites of target materials were used. The first were 1 cm^2 pieces of 103 μm thick aluminium foil (Al-1100), taken from flight spare foil from the *Stardust* mission (see Tsou et al., 2003, for details of the foils), and the second were typically 1 × 2 cm^2 blocks of SiO_2 aerogel. Two grades of aerogel were used in these experiments. For the synthetic olivines, the aerogel was not the density graded aerogel used in the *Stardust* mission but instead had a single, uniform density of ~30 mg/cm^3, which varied slightly from block to block. This is within the 5–50 mg/cm^3 range of the *Stardust* aerogel, and is slightly higher than the effective mean density experienced by particles during capture in the *Stardust* mission as reported by Burchell et al. (2009a). For the shot with San Carlos olivine we used a piece of flight grade, density gradient aerogel with the same density profile as that flown on *Stardust*. The range of the gun was evacuated to typically 0.5–1 mbar during each shot.

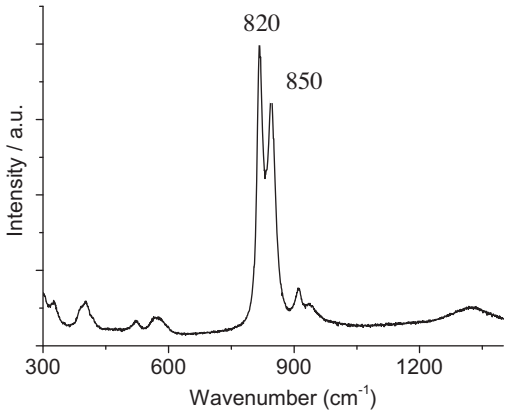

Fig. 1. Raman spectrum from raw sample of Fo_4. The distinctive peaks at 820 and 850 cm^{-1} are clearly visible.

3. RAW OLIVINE GRAINS

Raman spectra were obtained from the raw olivine samples using 2 min integration times (see Fig. 1 for an example). The two main peaks expected for olivine were clearly visible in each sample. Five to 10 grains per sample were examined, and a cross-plot made of the peak positions of the $P1$ and $P2$ peaks in each spectrum (Fig. 2). The results are similar to those given by Kuebler et al. (2006), with a clear trend reflecting variation in Mg–Fe content.

Following the approach of Kuebler et al. (2006) we first separately quantify the relation between Fo content and each of the two main olivine peaks. We label $P1$ as the peak position of the nominally 820 cm^{-1} peak, and $P2$ for the 850 cm^{-1} peak position. In Fig. 3, we show how Fo content varies with $P1$ and $P2$. These are fit with linear relations giving:

$$\text{Fo content} = -(5748 \pm 28) + (7.08 \pm 0.03)P1,\ r^2 = 0.9836, \quad (1)$$

and

$$\text{Fo content} = -(4090 \pm 20) + (4.88 \pm 0.02)P2,\ r^2 = 0.9930, \quad (2)$$

where r^2 is the square of the regression coefficient for the fits. Based on the 95% confidence bounds, we find that the uncertainty in these fits is equivalent to ±1.7 M units for Fo_{00}, falling to ±1.1 M units at Fo_{50} and rising again to ±1.7 M units at Fo_{100}. We next consider the linked relationship between $P1$, $P2$ and Fo content. This is shown on a 3-axis plot in Fig. 4. This was then fit with a parabolic function and the results are given in Table 2. We consider how accurate the predictions are from this combined fit by considering the residuals between the fit predictions and the true values. For the well constrained samples we find that at Fo_{40} the fit provides estimates which have a spread whose standard deviation is ±0.4 M units. Similarly at Fo_{80} and Fo_{100} we find the predictions have standard devi-

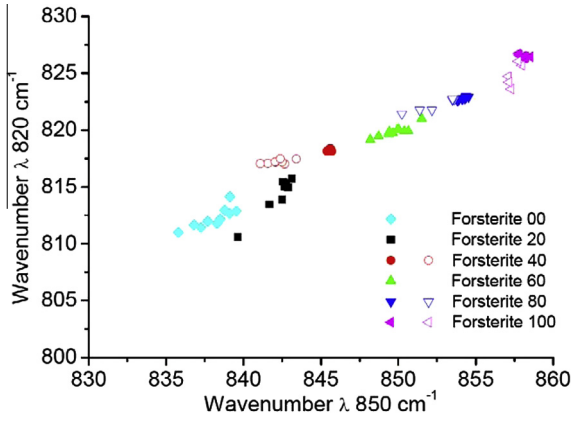

Fig. 2. A cross-plot of the positions of each of the two main olivine Raman peaks (nominally at 820 and 850 cm^{-1}, an example spectrum is shown in Fig. 1). Closed symbols are for the raw samples before any impact testing whilst open symbols are from residues in impact craters in aluminium. The various olivine samples are colour coded, and clearly fall into discrete sets. (For interpretation of the references to colour in this figure legend, the reader is referred to the web version of this article.)

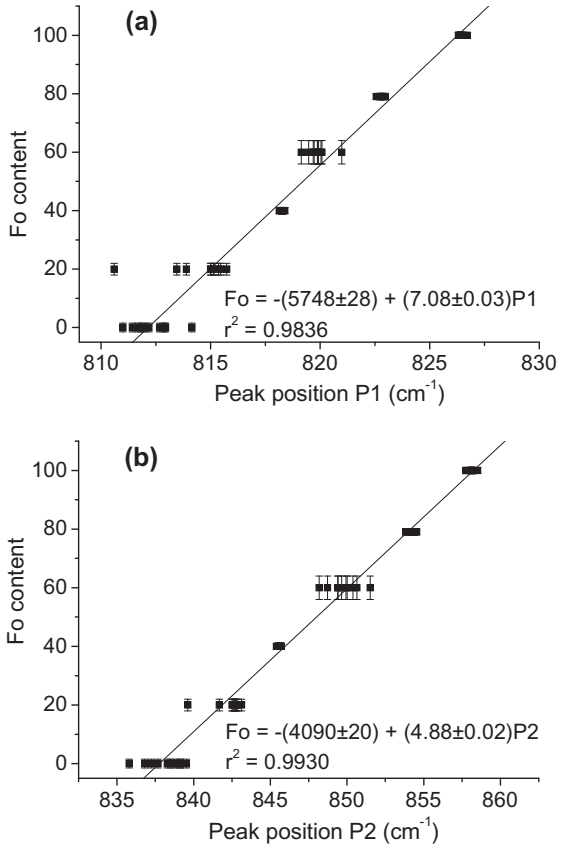

Fig. 3. The relation between molar Fo content and position of (a) $P1$, the nominally 820 cm^{-1} olivine Raman shift peak, and (b) $P2$, the nominally 850 cm^{-1} olivine Raman shift peak. A linear fit is shown in each case.

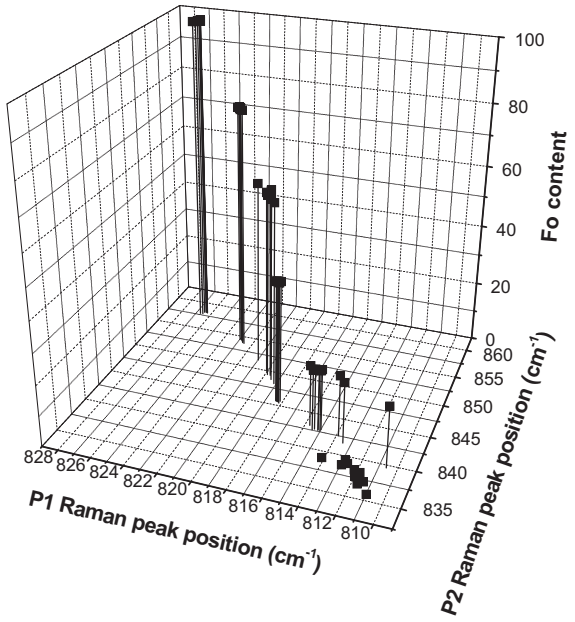

Fig. 4. Three dimensional plot showing the peak positions of the $P1$ and $P2$ olivine Raman peaks (x and y axes) as function of the Fo content (z axis) of the raw olivine grains.

ations of ±0.9 and ±0.5 M units, respectively. This is better than for the predictions using just $P1$ or $P2$ alone.

We then compare our results to those of Kuebler et al. (2006). In their paper, the position of $P1$ varied from 815 to 825 cm^{-1} as Fo content varied from 0 to 100, and $P2$ varied from 838 to 857 cm^{-1} over the same range. The data here are very similar for olivines above Fo_{20}, but at Fo_{00} our data lie at slightly lower wavenumbers than that of Kuebler et al. In consequence, our data can be fit by linear relations (Eqs. (1) and (2)) whereas Kuebler et al. used a 2nd order polynomial. Our data for Fo_{00} comprises measurements from 10 grains (compared to the 2 data points of Kuebler et al.) and show excellent reproducibility.

It has been shown by Mouri and Enami (2008) that the difference between $P1$ and $P2$ also depends on the Fo content. To test this here we show in Fig. 5 the parameter ω ($= P2 - P1$) vs. the Fo content (Fo#). A strong correlation can be seen. We fit it as:

$$\text{Fo\#} = -(371 \pm 20) + (14.5 \pm 0.7)\omega,\ r^2 = 0.8849. \quad (3)$$

Looking at the 95% confidence bands, we find that the uncertainty in molar content is ±5.8 M units for Fo_{00}, falling to ±3.2 units at Fo_{50} and rises to ±5.4 units at Fo_{100}. Although the fit seems good (and has a high regression coefficient), we note that Mouri and Enami (2008) used a polynomial to fit their data. Accordingly we find here:

$$\text{Fo\#} = (154 \pm 325) - (22.1 \pm 22.6)\omega + (0.634 \pm 0.392)\omega^2,\ r^2 = 0.8899. \quad (4)$$

This fit is not significantly better than the linear fit. Interestingly, although the data shown here in Fig. 5 agree with that of Mouri and Enami (2008) at high Fo content, they disagree at low Fo content (for comparison, in Fig. 5 the fit from Mouri and Enami (2008) is shown as a grey line).

4. RESULTS IN THE LABORATORY: IMPACTS ONTO ALUMINIUM

The olivine samples were fired onto target pieces of Al foil. The Fo_{20}, Fo_{40} and Fo_{80} samples were fired separately, whilst the Fo_{00}, Fo_{60} and Fo_{100} samples were fired together in a single shot (preliminary results had shown that these could be easily distinguished after impact, and thus their simultaneous use could eliminate the potential variation of velocity between shots). The measured impact speed in each shot is given in Table 1. After impact, the foils underwent preliminary SEM-EDX analysis in a similar way to that reported in Wozniakiewicz et al., (2009). This located impact craters, confirmed that the residue in a crater was from an olivine, and was able to distinguish which type of olivine had made each crater. Example craters are shown in Fig. 6.

Given that the olivine samples with the best constrained compositions were Fo_{40}, Fo_{80} and Fo_{100}, we focussed on these residues when analysing the impact craters. The craters chosen were typically 50 μm diameter, which, given the impactor-crater size calibration of Kearsley et al. (2006), suggests impactor sizes of order 10–12 μm. This is well below the original size of the grains, agreeing with the observation that the fragile raw grains broke up due to handling and acceleration in the gun. The Raman spectra were obtained in 2 or 5 min periods (the latter was used when the signal to noise was poor). The data for the cross-plot of the positions of the two main Raman peaks is shown in Fig. 2 for the 3 selected samples (Fo_{40}, Fo_{80} and Fo_{100}), along with the equivalent data for all the raw samples.

Table 2
Coefficients for parabolic fits to the positions of the two main olivine peaks (labelled $P1$ and $P2$) as a function of Fo_x content. The fit is of the form $x = a + b \times P1 + c \times P2 + d \times P1^2 + e \times P2^2$. The goodness of each fit is given by the square of the regression coefficient (r^2). The values are given to either 2 d.p. or 5 s.f. as the results of the formula are sensitive at that level.

	a	b	c	d	e	r^2
Olivine (raw)	62623.4	361.94	196.700	0.22181	0.11365	0.9881
Olivine crater residues	−332771	−282.545	1095.498	0.16715	−0.6643	0.9673
Olivine in aerogel	−80040	−229.137	406.354	0.13889	−0.23638	0.8690

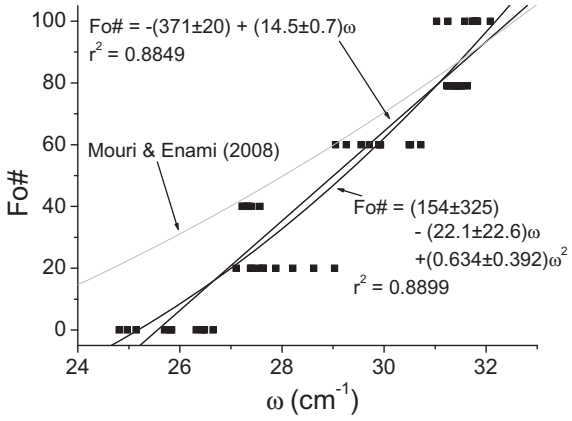

Fig. 5. The difference in the peak positions ω (defined as $P2 - P1$) is shown plotted vs. Fo content. This is fit with both linear and polynomial functions (dark lines, see text for details) and for comparison a fit from Mouri and Enami (2008) is shown in grey.

The data for each peak position ($P1$ and $P2$) versus Fo content are shown in Fig. 7. Again we fit with linear functions and obtain:

$$\text{Fo content} = -(6178 \pm 58) + (7.61 \pm 0.07)P1,\ r^2 = 0.9701, \quad (5)$$

and

$$\text{Fo content} = -(3200 \pm 30) + (3.85 \pm 0.04)P2,\ r^2 = 0.9825. \quad (6)$$

By considering the 95% confidence bounds in the fits, we find that at Fo_{40} the uncertainty on Fo content is ± 3.4 M units, falling to ± 2.1 M units at Fo_{65} and rising again to ± 3.4 M units at Fo_{100}. These uncertainties are twice those found for the raw grains.

We next consider the linked relationship between $P1$, $P2$ and Fo content. This is shown on a 3-axis plot in Fig. 8. This is then fit with a parabolic function, with the results given in Table 2. We again consider how accurate the predictions are from this combined fit by considering the spread in the fit predictions vs. the true values. At Fo_{40} the spread has a standard deviation of ± 1.4 M units. Similarly at Fo_{80} and Fo_{100} we find the predictions have spreads with standard deviations of 5.1 and 1.2 M units, respectively. At the higher and lower Fo values this is better than the individual fits, but is worse at intermediate values.

It is apparent from Fig. 2 and Fig. 7 that a shift in peak positions has occurred for the residue compared to the original grains. For $P1$, the mean peak position has shifted downward by approximately ~ 1 cm^{-1} at Fo_{100}, but decreasing to ~ 0.5 cm^{-1} at Fo_{40}. This would lead to an underestimate of the Fo content of 10 and 5 M units, respectively. $P2$ also shifts downwards, but with a different trend, shifting downwards by ~ 1 cm^{-1} at Fo_{100}, but increasing to ~ 4 cm^{-1} at Fo_{40}. This would lead to an underestimate in Fo content of 5 at high Fo values, but a larger underestimate of 25 M units at lower values. It is clear that if no correction were made to the residue data and the original raw grain calibration had been used to obtain Fo content, then a potentially significant error could arise.

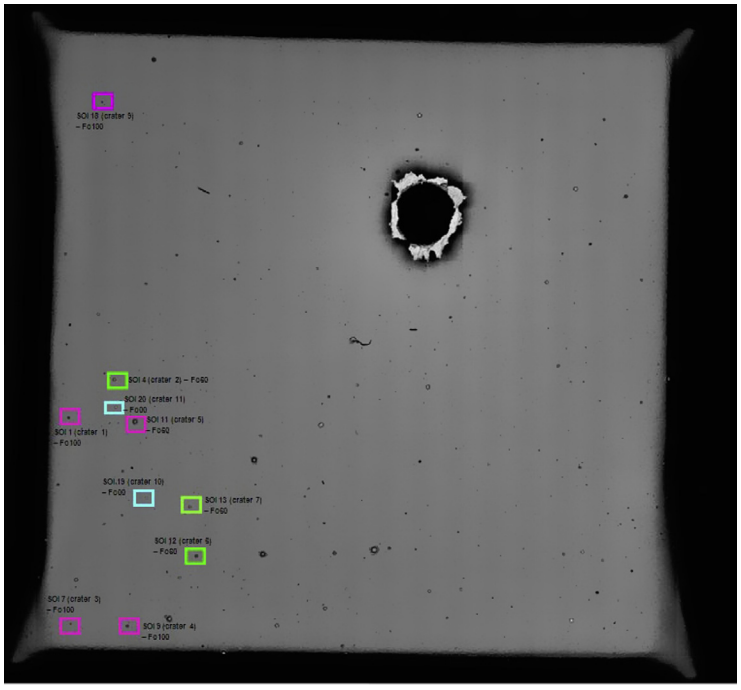

Fig. 6. Example of an aluminium foil after impact. The foil was 1×1 cm^2 in size. The large crater (upper right quadrant) was made by part of the sabot. The craters (mostly lower left quadrant) marked by square boxes were all identified by the residue as arising from impacts by olivines and the Fo_{xx} content determined by EDX.

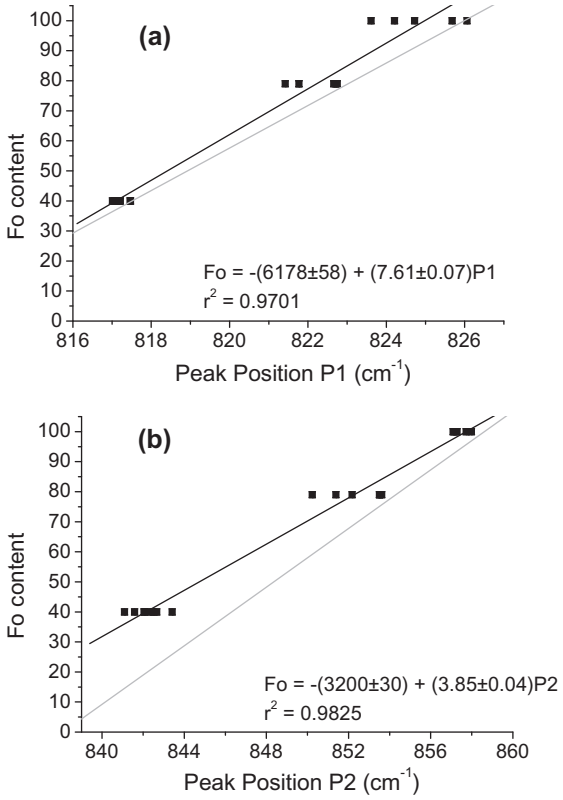

Fig. 7. The relation between molar Fo content and position of (a) *P*1, the nominally 820 cm^{-1} olivine Raman shift peak, and (b) *P*2, the nominally 850 cm^{-1} olivine Raman shift peak for residue in impact craters in aluminium foil. In each case, a linear fit is shown (black line, with parameters given in the figure), plus a light grey line shows the equivalent fit from the raw grains in Fig. 3. A shift can be seen for both *P*1 and *P*2.

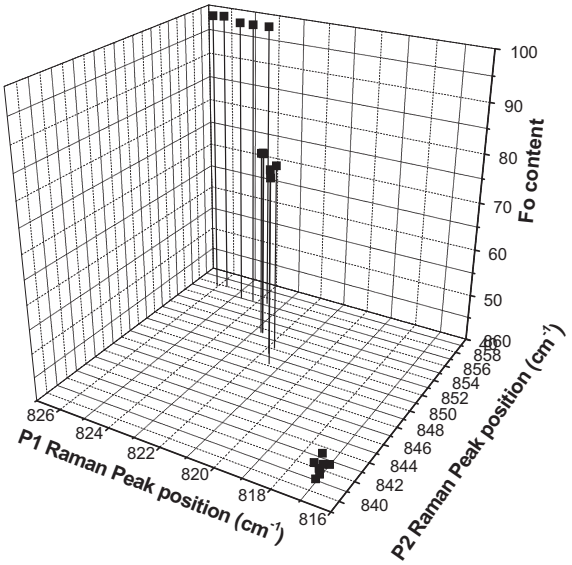

Fig. 8. Three dimensional plot showing the Fo content (*z* axis) as function of the peak positions of the *P*1 and *P*2 olivine Raman peaks (*x* and *y* axes) in the residues in the impact craters on aluminium foil.

We also plot the relationship between ω and Fo content (Fig. 9). We make a linear fit and obtain:

$$\mathrm{Fo} = -(172 \pm 11) + (8.50 \pm 0.39)\omega,\ r^2 = 0.9548. \quad (7)$$

This fit is shown as a black line in Fig. 9. Based on the 95% confidence bands we find that at Fo_{40} the molar uncertainty is ±4.1, falling to ±2.5 at Fo_{80} and then increasing slightly to ±3.8 at Fo_{100}. These uncertainties are slightly worse than those for using *P*1 and *P*2 separately. We also show for comparison the linear fit obtained from a similar plot for the raw olivine grains (grey line). It can be seen that there is a significant shift between the two fits at low Fo contents indicating the need for a correction to be applied when analysing residues in craters.

5. RESULTS IN THE LABORATORY: IMPACTS INTO AEROGEL

This work focussed on firing the 3 well controlled olivine samples (Fo_{40}, Fo_{80} and Fo_{100}) into aerogel of density ~30 mg/cm^3 (impact speeds given in Table 1). In addition, a sample of San Carlos olivine (Fo_{92}) was also fired into a piece of *Stardust* flight grade aerogel.

Note that all the olivine grains captured in the aerogel samples were observed in situ, with no attempt to remove the captured grains. Instead the captured grains, which were at the end of long narrow, carrot-shaped tracks (see Burchell et al., 2008a for a discussion of track morphology), were left in the aerogel during analysis by the Raman microscope. The tracks were typically a few millimetres to a few centimetres in length, and the captured grains were viewed from the side through a few mm of aerogel. The signal integration times were 8 min, significantly longer than that for the raw grains. In Fig. 10, an example Raman spectrum for Fo_{40} is shown for a sample observed in situ in aerogel. Spectra like this were obtained for multiple grains in each shot and were fit (as described earlier) to obtain the

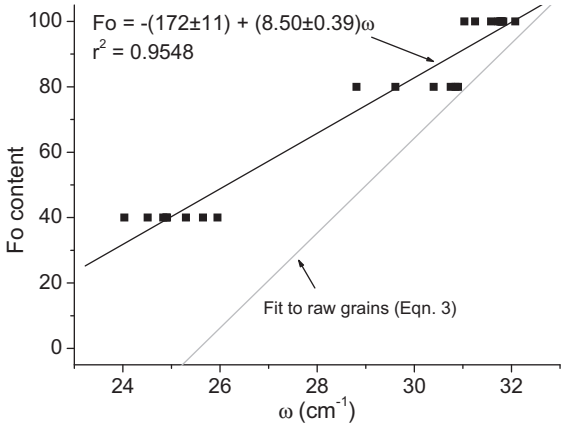

Fig. 9. The difference in the peak positions ω (defined as *P*2 − *P*1) is shown plotted vs. Fo content for olivine residues found in impact craters. This is fit with a linear function (dark line, see Eq. (7) in the text for details) and for comparison we show the fit to raw olivine grains (Eq. (3)).

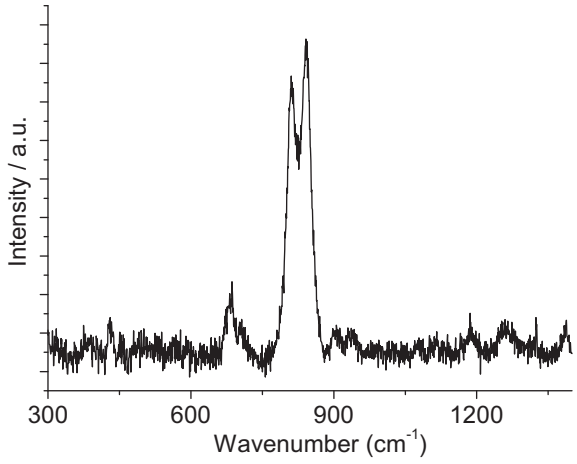

Fig. 10. Raman spectra from Fo_{40} grain captured in aerogel after impact at 6.01 km s^{-1}. (This can be compared to the spectrum from a Fo_{40} raw grain in Fig. 1).

peak positions. The resulting cross-plot of peak positions for the two main peaks is shown in Fig 11.

The results from aerogel show much greater dispersion than the residues in the Al-1100 foil craters, presented in the previous section. With the synthetic olivines, the position of the *P*1 peak shows both increases and decreases in its wavenumber, over a range of −10 to +4 cm^{-1}. The location of the *P*2 peak only shows a mean downward shift, of up to 10 cm^{-1}. The San Carlos olivine (which was initially well constrained in its Raman signature), underwent a downward shift of both peaks which brings it into the range of the Fo_{60} sample (which had a maximum composition of Fo_{67}). There is thus a potential shift of up to 20 M units in the Mg:Fe assignment. However, it should be noted that the shift does not lie along the curve defined by the original raw samples. The data for the grains after capture seems to lie (on average) on a displaced curve which is above the original trend at Fo_{100} and below at $<Fo_{80}$. However, there is substantial scatter in these data. The data for the San Carlos olivine fit well with the trend of the other samples. This suggests the use of density graded aerogel will not alter the results significantly. Accordingly we combine it with the other samples in the rest of this analysis.

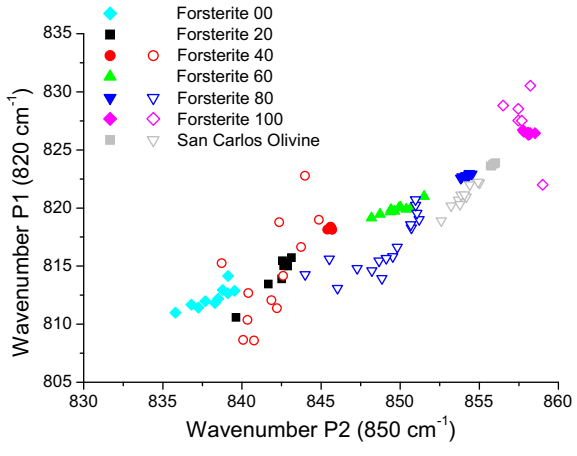

Fig. 11. The cross-plot of the positions of the two main olivine Raman peaks. The original data from the raw grains is shown with solid symbols. Data from grains captured in aerogel at 6.1 km s^{-1} are shown as open symbols. Note the presence of an additional olivine sample (San Carlos) with Fo_{92}.

As before we show the positions of the *P*1 and *P*2 peaks separately versus Fo content (Fig. 12). Unlike previously, a linear fit is not suitable to describe the data. Accordingly we applied 2nd order polynomial fits to the data in Fig. 12 and obtained:

$$\text{Fo content} = -70934 + 170.70P1 - 0.10255P1^2,\ r^2 = 0.4897, \quad (8)$$

and:

$$\text{Fo content} = -102581 + 238.24P2 - 0.13819P2^2,\ r^2 = 0.8478. \quad (9)$$

It can be seen from the fits, and as indicated by the regression coefficient, that the fit to the data for *P*1 (Fig 12a) is not very good. This occurs because there is large

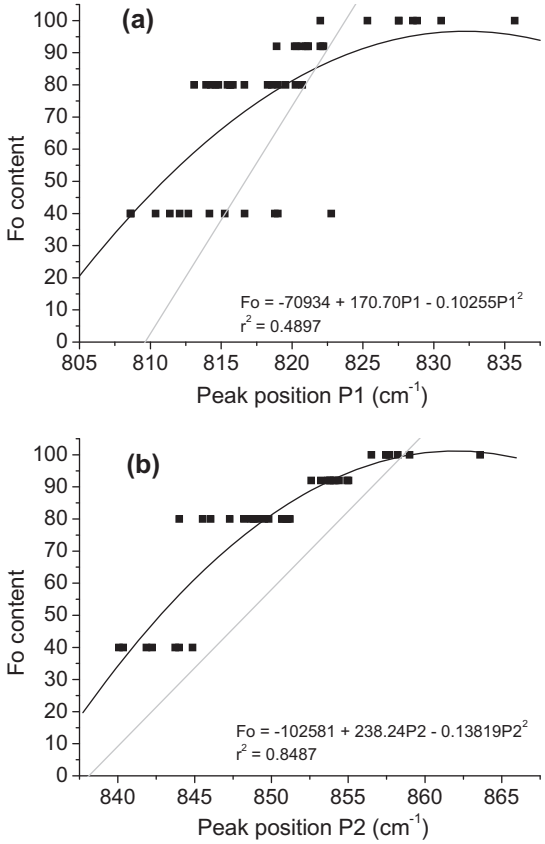

Fig. 12. The relation between molar Fo content and position of (a) *P*1, the nominally 820 cm^{-1} olivine Raman shift peak, and (b) *P*2, the nominally 850 cm^{-1} olivine Raman shift peak for olivine particles captured in aerogel at 6.1 km s^{-1}. In each case, a polynomial fit is shown (black line, with parameters given in the figure), plus a light grey line shows the fit from the raw grains in Fig. 3. A shift can be seen for both *P*1 and *P*2.

scatter on the data within each sample. Other fits can give a better regression coefficient, indicating a mathematically better fit, but they tend to exceed Fo_{100} at intermediate values of *P*1 and then fall to low Fo values at high values of *P*1. Given that this is not physical we exclude these fits as not valid. By contrast, the fit to the *P*2 values is a better one, with less scatter on the data. For *P*1, by considering the 95% confidence bounds in the fit, we find that at Fo_{40} the uncertainty on Fo content is ±6.5 M units, falling to ±5.3 M units at Fo_{80} and rising to ±13.0 M units at Fo_{100}. This reflects that in this case the fit is less certain at high Fo values. By contrast, for *P*2 we find that at Fo_{40} the uncertainty on Fo content is again ±6.5 M units, falling to ±2.9 M units at Fo_{80} and rising again to just ±3.8 M units at Fo_{100}. This reflects the better quality of the fit to the data. In the best case (*P*2) the uncertainties are only slightly worse than those for the residues in the impact craters.

In both cases, the captured grains have, on average, the same position for *P*1 and *P*2 for Fo_{100}, but at lower Fo contents have undergone a reduction in the position of *P*1 and *P*2, which, if not allowed for, would have resulted in a reduction of 15–30 in apparent Fo content.

A 3D scatter plot of the data from the samples captured in aerogel is shown in Fig. 13. We again fit with a parabola and the results are given in Table 2. By comparing the predicted values with the known true values we find that at Fo_{40} the values have a spread with a standard deviation of ±4.6) molar units. At Fo_{80}, Fo_{92} (the San Carlos olivine) and Fo_{100} we find the predictions have standard deviations of ±8.8, ±1.1 and ±1.6 M units, respectively. At the higher Fo values this is notably better than the individual *P*1 or *P*2 fit predictions, but is worse at Fo_{80}.

6. ANALYSIS OF A *STARDUST* COMETARY DUST IMPACT CRATER

The *Stardust* mission returned samples to Earth in 2006 and several aluminium foils were removed and scanned for craters; see Kearsley et al. (2008) for a report on the seven largest craters and Price et al. (2010) for a report on the sub-10 μm impactors. In this context, large craters are ones of size >50 μm and were likely to have required impactors of >10–12 μm size. It is the largest *Stardust* craters that are comparable in size to those studied in the laboratory, and accordingly we obtained two of these for Raman analysis.

The first crater was C2029W1 (see Kearsley et al., 2008 for details of the naming convention which relate to the location of the parent foil on the dust collector). SEM-EDX analysis had previously indicated that this was a residue rich crater. Its complex shape (see Fig. 14) suggests that a dust grain with a multi-component, possibly porous structure was involved in the impact. As shown in Fig. 14, one region of the crater was identified by SEM-EDX as having an elemental composition indicative of olivine. Accordingly this region, along with several others chosen randomly across the crater, was subject to Raman analysis. Spectra were obtained with integration times ranging from several minutes to 1 h. However, no trace of any distinct

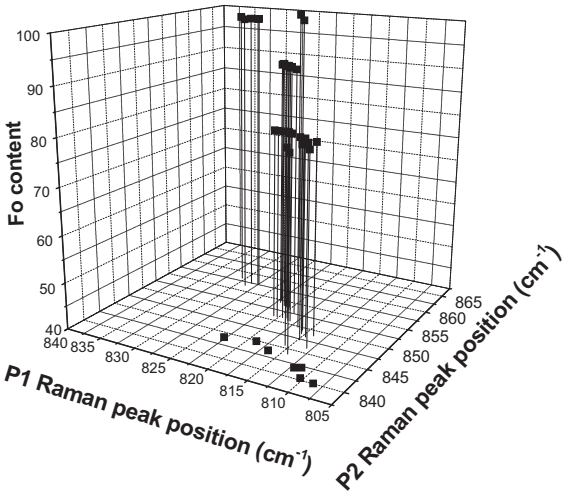

Fig. 13. Three dimensional plot showing the Fo content (*z* axis) as function of the peak positions of the *P*1 and *P*2 olivine Raman peaks (*x* and *y* axes) of olivine grains after capture in aerogel at 6.1 km s^{-1}.

peaks in any of the Raman spectra was found. It is possible that the residue is composed of many fine grained mixtures of different minerals at the sub-micron scale, or that if any residue survived un-mixed it may no longer be crystalline. Both could explain the lack of any recognisable mineral peaks in the Raman spectra.

The second crater studied was C2086N1 (see Fig. 15). This was a simple bowl-shaped crater which SEM-EDX had suggested was lined with residue that had an elemental composition consistent with that of an olivine impactor. The relatively large depth/diameter ratio of this crater suggests it was made by either a spherical projectile with bulk density significantly greater than that of olivine, or was a 'rod' penetration by an elongate impactor, with lower bulk density that could be consistent with olivine. Several Raman spectra obtained from various sites inside the crater exhibited olivine peaks located at 824.4 ± 0.5 and 857.0 ± 0.5 cm^{-1}. An example spectrum (with a 5 min integration time) is shown in Fig. 16. Based on the SEM and Raman results we suggest that the crater was created by impact of an irregularly shaped olivine rich grain.

We compared the Raman peak positions with those found for experimental crater residues (Fig. 2); by eye, the result for C2086N1 lies between the Fo_{80} and Fo_{100} data sets. The closest data set in the laboratory analysis was Fo_{100}, (which is very close to SEM-EDX of the residue). If we apply the post-shock calibrations found individually for *P*1 and *P*2 in Eqs. (5) and (6), we find estimates of Fo molar content of 95.7 and 99.5, respectively. But, if we had used the calibration from the raw olivine grains (Eqs. (1) and (2)), we would have obtained Fo molar contents of 88.8 and 92.1, respectively, and we would have underestimated the Fo content by approximately 7 M units. Use of the calibrations with a combined fit to *P*1 and *P*2 (the polynomial fit results in Table 2) yields an estimate of Fo content of 96.1 (accurate to 1.2 M units) if the post-shock crater residue data is used, but only 92.1 if the data from

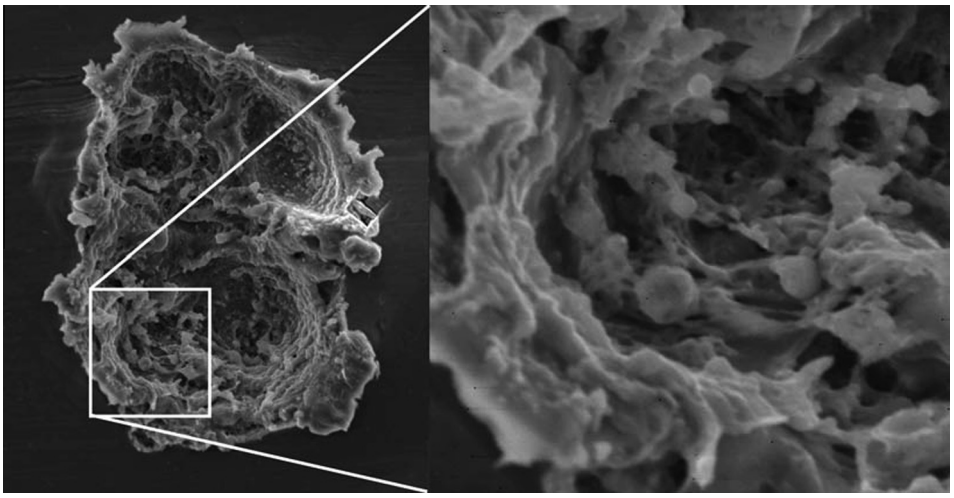

Fig. 14. Stardust cometary crater C2029W1. The left panel shows the full crater, whose maximum extent is some 167 μm × 133 μm (lip to lip) and depth (below the ambient surface plane) is some 34 μm. SEM-EDX analysis found plentiful traces of residue, and the enlarged region (right panel) had residue whose elemental composition was compatible with olivine. See Kearsley et al. (2008) for more details.

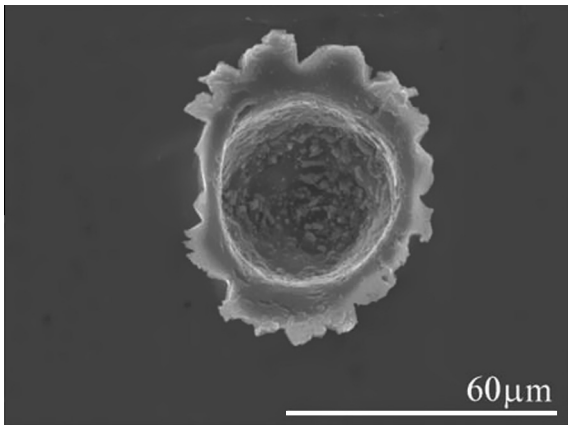

Fig. 15. Stardust cometary crater C2086N1. This is a bowl-shaped crater, indicative of a single grain, well consolidated impactor. See Kearsley et al. (2008) for more details. The texture lining the crater is a visual indicator of the survival of plentiful impactor reside, which SEM-EDX suggests has an elemental composition compatible with olivine. The crater width (lip to lip) is 57 μm, but it is relatively deep at 34 μm. This large depth to diameter ratio suggests either spherical impactor notably denser than olivine, or impact by an elongated impactor of lower density.

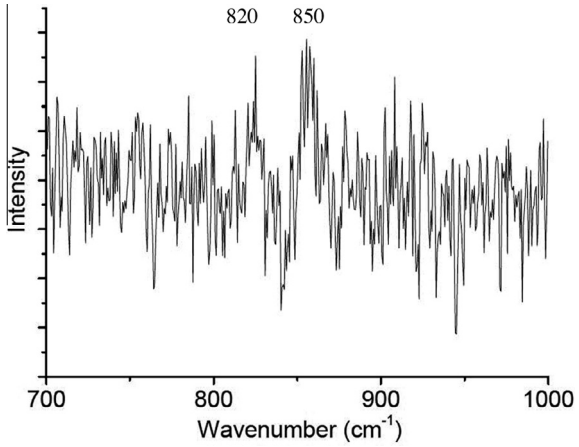

Fig. 16. Raman spectra from residue in Stardust cometary crater C2086N1. The signal to noise is not good, but the olivine nominal 820 and 850 cm^{-1} peaks are visible (labelled 820 and 850, respectively).

the raw grains is used (an underestimate of ~4 M units). If we estimate the Fo content using the ω relationship of Eq. (3) we find a Fo molar content of 104.9, in excess of 100%.

We thus find that this crater was probably made by a non-spherical, elongated particle (hence the multi-pit, shallow crater shape) which contained an olivine sub-grain of type $Fo_{96–100}$, with a best estimate of $Fo_{96±1}$. Based on the original SEM-EDX analysis, Kearsley et al. (2008) suggested the sub-grain was Fo_{97}. This was without any correction for alteration that might be introduced by the dust collection method. Wozniakiewicz et al. (2012a) have since shown that single grain olivines of high Fo content do not undergo significant modification of elemental ratio as a result of impact at 6.1 km s^{-1} into aluminium foil; thus SEM-EDX results for such materials are reliable indicators of original composition. The Raman and SEM-EDX results are thus in agreement, confirming the presence of olivine with a very high Fo molar content in this crater.

7. ANALYSIS OF A *STARDUST* COMETARY AEROGEL TRACK

Grains from two *Stardust* tracks were obtained and subject to Raman analysis. One grain was still in situ in aerogel, the other had been extracted and pressed into gold. However, it rapidly became apparent that these grains had an iron-oxide composition and not olivine. Accordingly, their analysis has been reported elsewhere (Bridges et al., 2010).

8. DISCUSSION

That mineralogy can be obtained from grains impacting aluminium foil at 6.1 km s^{-1}, is a result that has greatly benefited the *Stardust* analysis. SEM studies of mineralogy, based on EDX observations of elemental composition have been reported elsewhere (e.g. Kearsley et al., 2008; Price et al., 2010), as have studies of possible biases introduced by the impact and subsequent analysis methods (Wozniakiewicz et al., 2009, 2012a). The olivine residue identified here in a *Stardust* aluminium foil crater (C2086N1), produces consistent results from both the Raman and SEM-EDX analyses. If only Raman spectroscopy with calibrations based on raw grains (and not crater residues) had been used to identify the molar content, then this would have been underestimated by 7 M units if a single Raman peak had been used, and underestimated by 4 M units if the positions of both main olivine peaks were used. This discrepancy would have been even greater if the olivine had been of a lower Fo content.

A separate Raman study of different *Stardust* cometary grains captured in aerogel by Wopenka (2012) has reported the detection of a grain (spot γ on particle C2092,6,80,51,0) containing $Fa_{30}Fo_{70}$. The study did not make any correction for alteration of the Raman signature during particle capture, and compared the spectra obtained from *Stardust* grains directly to those from raw grains of synthetic olivines, using the raw olivine calibration of Kuebler et al. (2006). This suggested a Fo molar content of 70. If we use our raw grain calibrations to interpret the same *Stardust* particle data, we obtain Fo molar contents of 57.6 from *P*1, 72.6 from *P*2 and 70.3 from a combined fit to *P*1 and *P*2. Our best estimate is thus also a Fo molar content of 70, supporting the results of Wopenka (2012). This is not a surprise given the observation above that the Raman shifts obtained here for the raw olivine grains agree well with those reported by Kuebler et al. (2006). However, this does not allow for potential bias during capture, and if we use the calibrations obtained from grains captured in aerogel, our interpretation changes. If we use *P*1 alone we obtain a Fo molar content of 81.3 ± 5.3, with 88.6 ± 2.9 from *P*2, and 85.0 ± 8.8 from a combined fit. Thus based on the observations here, the mean predicted Fo content of this grain may be under-estimated by Wopenka (2012) by as much as 19 M units.

There are caveats however. The olivine particles used in the analysis here are discrete grains, which remain (relatively) intact at the ends of the aerogel tracks. In the nomenclature of Burchell et al. (2008a) these are Type A tracks, i.e. a long and slender track with a well-defined terminal grain at its end. The grain measured by Wopenka (2012) was from a bulbous track which was border-line Type B/C, i.e. with little, if any, evidence for significant terminal grains beneath the bulbous cavity. In addition, the grain studied was extracted from the wall of the bulbous cavity along its length and not from the end of the cavity. The grain measured by Wopenka (2012) may thus have experienced a different shock and thermal history to those used in this study. The corrected Fo content suggested here should therefore be taken as a preliminary assessment, which may require revision when closer analogues are available.

There is now an extensive literature on the nature of these Type B/C tracks. Burchell et al. (2008a) originally suggested that the bulbous cavities might be associated with vapour driven expansion from volatile rich impactors. By contrast, on theoretical grounds, Trigo-Rodríguez et al. (2008) assigned Type B tracks to impacts by weak impactors. Kearsley et al. (2009), demonstrated that bulbous tracks can be created experimentally by firing weakly bound mineral aggregates at aerogel, and also suggested that a mixture of fine grained material with a few larger components could be responsible for Type B tracks. More recent papers take these ideas further, showing and discussing examples of different track types from the *Stardust* mission itself (Joswiak et al., 2012) and from laboratory experiments (Kearsley et al., 2012). Fig. 14 of Kearsley et al. (2012) provides a scheme to associate track type with particle structure, but does not address crystallographic or compositional modification to the impacting particle components. During capture, the grains will have been shocked, and are likely to have intermingled with molten aerogel, this will have led to elevated temperatures at the surfaces of the grains. This applies to both terminal grains in the Type A track discussed here, and grains found in the walls of Type B/C tracks. We thus expect there will have been alteration to the Raman spectra of the captured grains (as shown here for single grains captured relatively intact). Indeed, the fine grain size of many probable aggregate components may have resulted in much more pervasive internal heating, melting and recrystallisation. A separate study is therefore needed on the multi-grain impactors which result in Type B, to determine if the resultant changes are the same magnitude or indeed greater than for coarse single grain impactors.

9. CONCLUSIONS

The value of Raman spectroscopy not just to identify olivine, but also to determine the molar concentration of Fe:Mg therein, was demonstrated by Kuebler et al. (2006) and here we concur. However, we also refine the application in demonstrating that even after impacts at speeds of ~6 km s^{-1}, we can still identify the molar content of olivine grains from the residue which lines impact craters in metal foils or from grains captured in aerogel.

We also show that there are changes in the relationship between the positions of the two main Raman peaks in olivine, as a result of the processes involved in capture on foil and aerogel at 6.1 km s^{-1}. This could introduce bias into the determination of the molar content, and should be a consideration in any analytical interpretation. Even in the most extreme case reported here (impacts onto aluminium, generating peak shock pressures of 85–90 GPa), there is crystalline olivine present in the residue. This had been reported previously (Burchell et al., 2008b), but with the caveat there was always the possibility it was newly crystallised, following complete shock melting of the projectile. Burchell et al. (2008b) argued that this was not the case, but that the material was a remnant of the original

crystalline mineral. Survival of structure was confirmed in a separate study of impacts of another silicate mineral (wollastonite) onto aluminium foil under very similar experimental conditions (Wozniakiewicz et al., 2012b). Here it was shown that residue in the impact craters even retained the original crystalline lattice orientation of the projectile material, which could not be explained by crystallization from an amorphous melt. Wozniakiewicz et al. (2012a) also showed that the composition of olivine residue within *Stardust* analogue impact craters showed no evidence of fractionation between the constituent chemical elements, and retained the pre-impact Mg:Fe ratio. Thus we also conclude that the changes in Raman spectra seen in the impact craters are the result of the strain imposed on the olivine crystalline lattice during the shock event, and are not the result of preferential loss of one element or the other from a melt created during impact.

Capture in aerogel, although associated with significantly lower shock pressures than impacts on metal foil, does induce surface modification of captured grains (with loss of material observed) and exposes the particles to high temperatures (wraps of "melted" aerogel have been observed around captured grains). In this case it is less clear if changes to the Raman spectra are the result of shock effects on the lattice, or could be due to preferential loss of one component versus another as a result of heating, or even recombination of elements from mixed precursors and subsequent growth of a new crystalline lattice structure (as seen in the fate of iron sulfide minerals during capture in aerogel, documented by Ishii et al., 2008). A separate analogue study is therefore still required to extract remains of a wide range of olivine projectile sizes from aerogel tracks, and to perform compositional analysis and crystallographic determination of their preservation state.

The work here is directly relevant to analysis of mineral grains captured in space via high speed impacts. In particular the NASA *Stardust* mission captured cometary dust grains via high speed impacts onto aluminium foils and SiO_2 aerogel. The published analyses of mineralogy of the Wild-2 cometary dust grains show that, amongst the identified olivine grains, there is a prevalence of Mg-rich olivines (Zolensky et al., 2006, 2008). Previous work on chondritic porous (CP) interplanetary dust particles (IDPs), has also shown that Mg-rich end members dominate amongst the crystalline anhydrous silicates (e.g. Bradley, 2003), and silicate grains (including olivine) observed in protoplanetary disks are also usually Mg-rich (although there are reports that in certain cases Fe can be favoured, see Olofsson et al., 2012).

Returned material from the *Stardust* mission has been analysed with a very wide range of techniques, with much use made of SEM-EDX techniques which give elemental compositions. These results are then compared to compositions of known minerals and a provisional identification made. A fuller identification requires structural investigation in synchrotron, or transmission electron microscopy of samples extracted from aerogel (for relatively large craters new extraction techniques are having to be developed to access the residue in the craters). An advantage of Raman analysis is that it not only identifies the mineral directly, it does so in situ and indicates that it is crystalline. However, as shown here, if appropriate corrections are not made, then there is the risk of error in assignment of the Fe:Mg content, which can be very significant for Mg molar ratio values of <0.8 or lower. It should be remembered however that the *Stardust* grains are often characterised as fine grained assemblages of many materials. The grains used here in our laboratory studies were larger single grain samples. Future studies will attempt to see what happens if we use fine grained samples in the laboratory experiments.

Documenting the detailed diversity of olivine (and pyroxene) composition is potentially a powerful tool (e.g. for comparison of the cometary dust particles collected from comet Wild 2 with other extraterrestrial materials, especially chondritic meteorites, Zolensky et al., 2008). Unfortunately, extraction of large numbers of grains from *Stardust* aerogel tracks for analysis by analytical electron microscopy is both very time-consuming and destructive. In situ synchrotron X-ray fluorescence analysis and diffraction studies are very powerful means to recognise and characterise silicate grains within tracks, but may be hampered by restrictions on access to expensive facilities. Raman spectroscopy thus seems an ideal non-destructive tool for early application to a large number of samples, but requires an understanding of capture-related modification of Raman signatures before reliable Fo:Fa ratios can be determined.

ACKNOWLEDGEMENTS

We thank STFC (UK) for funding the *Stardust* analysis and light gas gun work at Kent. N.F. thanks the Univ. of Kent alumni for funding. We thank the *Stardust* team and NASA curatorial facility for access to samples.

REFERENCES

Brownlee D. E., Tsou P., Aleón J., Alexander C. M. O'D., Araki T., Bajt S., Baratta G. A., Bastien R., Bland P., Bleuet P., Borg J., Bradley J. P., Brearley A., Brenker F., Brennan S., Bridges J. C., Browning N., Brucato J. R., Brucato H., Bullock E., Burchell M. J., Busemann H., Butterworth A., Chaussidon M., Cheuvront A., Chi M., Cintala M. J., Clark B. C., Clemett S. J., Cody G., Colangeli L., Cooper G., Cordier P. G., Daghlian C., Dai Z., D'Hendecourt L., Djouadi Z., Dominguez G., Duxbury T., Dworkin J. P., Ebel D., Economou T. E., Fairey S. A. J., Fallon S., Ferrini G., Ferroir T., Fleckenstein H., Floss C., Flynn G., Franchi I. A., Fries M., Gainsforth Z., Gallien J.-P., Genge M., Gilles M. K., Gillet P., Gilmour J., Glavin D. P., Gounelle M., Grady M. M., Graham G. A., Grant P. G., Green S. F., Grossemy F., Grossman L., Grossman J., Guan Y., Hagiya K., Harvey R., Heck P., Herzog G. F., Hoppe P., Hörz F., Huth J., Hutcheon I. D., Ishii H., Ito M., Jacob D., Jacobsen C., Jacobsen S., Joswiak D., Kearsley A. T., Keller L., Khodja H., Kilcoyne A. L. D., Kissel J., Krot A., Langenhorst F., Lanzirotti A., Le L., Leshin L., Leitner J., Lemelle L., Leroux H., Liu M.-C., Luening K., Lyon I., MacPherson G., Marcus M. A., Marhas K., Matrajt G., Meibom A., Mennella V., Messenger K., Mikouchi T., Mostefaoui S., Nakamura T., Nakano T., Newville M., Nittler L. R., Ohnishi I., Ohsumi K., Okudaira K., Papanastassiou D. A., Palma R., Palumbo M. O., Pepin R. E., Perkins D., Perronnet M., Pianetta P., Rao W., Rietmeijer F., Robert F., Rost D., Rotundi A., Ryan R.,

Sandford J. A., Schwandt C. S., See T. H., Schlutter D., Sheffield-Parker J. A., Simionovici S., Sitnitsky S. I., Snead C. J., Spencer M. K., Stadermann F. J., Steele A., Stephan T., Stroud R., Susini J., Sutton S. R., Taheri M., Taylor S., Teslich N., Tomeoka K., Tomioka N., Toppani A., Trigo-Rodrıguez J. M., Troadec D., Tsuchiyama A., Tuzzolino A. J., Tyliszczak T., Uesugi K., Velbel M., Vellenga J., Vicenzi E., Vincze L., Warren J., Weber I., Weisberg M., Westphal A. J., Wirick S., Wooden D., Wopenka B., Wozniakiewicz P. A., Wright I., Yabuta H., Yano H., Young E. D., Zare R. N., Zega T., Ziegler K., Zimmerman L., Zinner E. and Zolensky M. (2006) Comet 81P/Wild 2 under a microscope. *Science* **314**, 1711–1716.

Bridges J. C., Burchell M. J., Changeka H. C., Foster N. J., Creighton J. A., Carpenter J. D., Gurman S. J., Franchi I. A. and Busemann H. (2010) Iron oxides in comet 81P/Wild 2 samples. *Meteorit. Planet. Sci.* **45**, 55–72.

Bradley J. P. (2003) Interplanetary dust particles. In *Meteorites, Comets and Planets: Treatise on Geochemistry*, vol. 1 (eds. A. M. Davis, H. D. Holland and K. K. Turekian). Elsevier-Pergamon, Oxford, pp. 690–711.

Burchell M. J. and Kearsley A. T. (2009) Short period Jupiter family comets after stardust. *Planet. Space Sci.* **57**, 1146–1161.

Burchell M. J., Cole M. J., McDonnell J. A. M. and Zarnecki J. C. (1999) Hypervelocity impact studies using the 2 MV van de graaf accelerator and two-stage light gas gun of the University of Kent at Canterbury. *Meas. Sci. Technol.* **10**, 41–50.

Burchell M. J., Creighton J. A., Cole M. J., Mann J. and Kearsley A. T. (2001) Capture of particles in hypervelocity impacts in aerogel. *Meteorit. Planet. Sci.* **36**, 209–221.

Burchell M. J., Creighton J. A. and Kearsley A. T. (2004) Identification of organic particles via Raman techniques after capture in hypervelocity impacts on aerogel. *J. Raman Spectrosc.* **35**, 249–253.

Burchell M. J., Graham G. and Kearsley A. (2006a) Cosmic dust collection in aerogel. *Annual Reviews of Earth and Planetary Science* **34**, 385–418.

Burchell M. J., Mann J., Creighton J. A., Kearsley A. T., Graham G. and Franchi I. A. (2006b) Identification of minerals and meteoritic materials via Raman techniques after capture in hypervelocity impacts on aerogel. *Meteorit. Planet. Sci.* **41**, 217–232.

Burchell M. J., Fairey S. A. J., Wozniakiewicz P., Brownlee D. E., Hörz F., Kearsley A. T., See T. H., Tsou P., Westphal A., Green S. F., Trigo-Rodrıguez J. M. and Domingúez G. (2008a) Characteristics of cometary dust tracks in Stardust aerogel and laboratory calibrations. *Meteorit. Planet. Sci.* **43**, 23–40.

Burchell M. J., Foster N. J., Kearsley A. T. and Creighton J. A. (2008b) Identification of mineral impactors in hypervelocity impact craters in aluminium by Raman spectroscopy of residues. *Meteorit. Planet. Sci.* **43**, 135–142.

Burchell M. J., Fairey S. A. J., Foster N. J. and Cole M. J. (2009a) Hypervelocity capture of particles in aerogel: dependence on aerogel properties. *Planet. Space Sci.* **57**, 58–70.

Burchell M. J., Foster N. J., Ormond-Prout J., Dupin D. and Armes S. P. (2009b) Extent of thermal ablation suffered by model organic microparticles during aerogel capture at hypervelocities. *Meteorit. Planet. Sci.* **44**, 1407–1420.

Chopelas A. (1991) Single crystal Raman spectra of fosterite, fayalite and monitcellite. *Am. Min.* **76**, 1101–1109.

Durden D. J., McMillan P. F. and Wolf G. H. (1993) Raman study of the high pressure behaviour of forsterite (Mg2SiO4) crystal and glass. *Am. Min.* **78**, 1143–1148.

Fries M., Burchell M., Kearsley A. and Steele A. (2009) Stardust analogue study using hypervelocity aerogel capture of coal samples – using particle exteriors to understand capture alteration. *Meteorit. Planet. Sci.* **44**, 1465–1474.

Henning T. (2010) Cosmic silicates. *Annual Review of Astronomy and Astophysics* **48**, 21–46.

Hörz F., Cintala M. J., See T. H. and Nakamura-Messenger K. (2009) Penetration tracks in aerogel produced by Al_2O_3 spheres. *Meteorit. Planet. Sci.* **44**, 1243–1264.

Ishii H. A., Bradley J. P., Dai Z. R., Chi M., Kearsley A. T., Burchell M. J., Browning N. D. and Molster F. (2008) Comparison of comet 81P/Wild 2 dust with interplanetary dust from comets. *Science* **37**(319), 447–450.

Joswiak D. J., Brownlee D. E., Matrajt G., Westphal A. J., Snead C. J. and Gainsforth Z. (2012) Comprehensive examination of large mineral and rock fragments in Stardust tracks; mineralogy, analagous extraterrestrail materials, and source regions. *Meteorit. Planet. Sci.* **47**, 471–524.

Kearsley A. T., Burchell M. J., Hörz F., Cole M. J. and Schwandt C. S. (2006) Laboratory simulations of impacts upon aluminium foils of the Stardust spacecraft: calibration of dust particle size from comet Wild2. *Meteorit. Planet. Sci.* **41**, 167–180.

Kearsley A. T., Borg J., Graham G. A., Burchell M. J., Cole M. J., Leroux H., Bridges J. C., Hörz F., Wozniakiewicz P. J., Bland P. A., Bradley J. P., Dai Z. R., Teslich N., See T., Hoppe P., Heck P. R., Huth J., Stadermann F. J., Floss C., Marhas K., Stephan T. and Leitner J. (2008) Dust from comet Wild 2: interpreting particle size, shape, structure and composition from impact features on the Stardust aluminium foils. *Meteorit. Planet. Sci.* **43**, 41–74.

Kearsley A. T., Burchell M. J., Price M. C., Graham G. A., Wozniakiewicz P. J., Cole M. J., Foster N. J. and Teslich N. (2009) Interpretation of Wild 2 dust fine structure: comparison of Stardust aluminium foil craters to three dimensional shape of experimental impacts by artificial aggregate particles and meteorite powders. *Meteorit. Planet. Sci.* **44**, 1489–1510.

Kearsley A. T., Burchell M. J., Price M. C., Cole M. J., Wozniakiewicz P. J., Ishii H. A., Bradley J. P., Fries M. and Foster N. J. (2012) Experimental impact features in Stardust aerogel: how track morphology reflects particle structure, composition and density. *Meteorit. Planet. Sci.* **47**, 737–762.

Kuebler K., Jolli B. L., Wang A. and Haskin L. A. (2006) Extracting olivine (Fo–Fa) compositions from Raman spectral peak positions. *Geochim. Cosmochim. Acta* **70**, 6201–6222.

Mouri T. and Enami M. (2008) Raman spectroscopic study of olivine-group minerals. *Journal of Minealogical and Petrological Sciences* **103**, 100–104.

Olofsson J., Juhasz A., Henning Th., Mutschke H., Tamanai A., Moor A., Abraham P. (2012) Transient dust in warm debris disks: detection of Fe-rich olivine grains. *Astron. Astrophys.* **542**, article number: A90. http://dx.doi.org/10.1051/0004-6361/201118735.

Noguchi T., Nakamura T., Kumara K., Yano H., Sugita S. and Burchell M. J. (2007) Thermal alteration of hydrated minerals during hypervelocity capture to silica aerogel at the flyby speed of Stardust. *Meteorit. Planet. Sci.* **42**, 357–372.

Price M. C., Kearsley A. T., Burchell M. J., Hörz F., Borg J., Bridges J. C., Cole M. J., Floss C., Graham G., Green S. F., Hoppe P., Leroux H., Marhas K. K., Park N., Stroud R., Stadermann F. J. and Wozniakiewicz P. J. (2010) Comet 81P/Wild 2: the size distribution of finer (sub 10 micrometre) dust collected by the Stardust spacecraft. *Meteorit. Planet. Sci.* **45**, 1409–1428.

Rotundi A., Baratta G. A., Borg J., Brucato J. R., Busemann H., Colangeli L., D'Hendecourt L., Djouadi Z., Ferrini G., Franchi I. A., Fries M., Grossemy F., Keller L. P., Mennella V., Nakamura K., Nittler L. R., Palumbo M. E., Sandford S. A.,

Steele and Wopenka B. () Combined micro-Raman, micro-infrared, and field emission scanning electron microscope analyses of comet 81P/Wild 2 particles collected by Stardust. *Meteorit. Planet. Sci.* **43**, 367–397.

Sandford S. C. et al. (2006) Organics captured from the comet Wild 2 by the Stardust spacecraft. *Science* **314**, 1720–1724.

Trigo-Rodríguez J., Domínguez G., Burchell M. J., Hörz F. and Lorca J. (2008) Bulbous tracks arising from hypervelocity capture in aerogel. *Meteorit. Planet. Sci.* **43**, 75–86.

Tsou P., Brownlee D. E., Sandford S. A., Hörz F. and Zolensky M. E. (2003) Wild-2 and interstellar sample collection and Earth return. *J. Geophys. Res.* **108**(E10), 8113, http://dx.doi.org/10.1029/2003JE002109.

Wopenka B. (2012) Raman spectroscopic investigation of two grains from comet 81P/Wild 2: information that can be obtained beyond the presence of sp2-bonded carbon. *Meteorit. Planet. Sci.* **47**, 565–584.

Wozniakiewicz P. J., Kearsley A. T., Burchell M. J., Foster N. J., Cole M. J., Bland P. A. and Russell S. S. (2009) Analyses of residues resulting from laboratory impacts into aluminium 1100 foil: implications for stardust crater analyses. *Meteorit. Planet. Sci.* **44**, 1541–1560.

Wozniakiewicz P. J., Ishii H. A., Kearsley A. T., Burchell M. J., Bradley J. P., Price M. C., Teslich N., Lee M. R. and Cole M. J. (2012a) Stardust impact analogues: resolving pre- and post-impact mineralogy in stardust Al foils. *Meteorit. Planet. Sci.* **47**, 708–728.

Wozniakiewicz P. J., Kearsley A. T., Ishii H. A., Burchell M. J., Bradley J. P., Teslich N., Cole M. J. and Price M. C. (2012b) The origin of crystalline residues in Stardust Al foils: surviving cometary dust or crystallized impact melts? *Meteorit. Planet. Sci.* **47**, 660–670.

Zolensky M. E., Zega T. J., Yano H., Wirick S., Westphal A. J., Weisberg M. K., Weber I., Warren J. L., Velbel M. A., Tsuchiyama A., Tsou P., Toppani A., Tomioka N., Tomeoka K., Teslich N., Taheri M., Susini J., Stroud R., Stephan T., Stadermann F. J., Snead C. J., Simon S. B., Simionovici A., See T. H., Robert F., Rietmeijer F. J. M., Rao W., Perronnet M. C., Papanastassiou D. A., Okudaira K., Ohsumi K., Ohnishi I., Nakamura-Messenger K., Nakamura T., Mostefaoui S., Mikouch T., Meibom A., Matrajt G., Marcus M. A., Leroux H., Lemelle L., Le L., Lanzirotti A., Langenhorst F., Krot A. N., Keller L. P., Kearsley A. T., Joswiak D., Jacob D., Ishii H., Harvey R., Hagiya K., Grossman L., Grossman J. N., Graham G. A., Gounelle M., Gillet P., Genge M. J., Flynn G., Ferroir T., Fallon S., Ebel D. S., Dai Z. R., Cordier P., Clark B., Chi M., Butterworth A. L., Brownlee D. E., Bridges J. C., Brennan S., Brearley A., Bradley J. P., Bleuet P., Bland P. A. and Bastien R. (2006) Mineralogy and petrology of comet 81P/Wild 2 nucleus samples. *Science* **314**, 1735–1739.

Zolensky M., Nakamura-Messenger K., Rietmeijer F., Leroux H., Mikouchi T., Ohsumi K., Simon S., Grossman L., Stephan T., Weisberg M., Velbel M., Zega T., Stroud R., Tomeoka K., Ohnishi I., Tomioka N., Nakamura T., Matrajt G., Joswiak D., Brownlee D., Langenhorst F., Krot A., Kearsley A., Ishii H., Graham G., Dai Z. R., Chi M., Bradley J., Hagiya K., Gounelle M. and Bridges J. (2008) Comparing Wild 2 particles to chondrites and IDPs. *Meteorit. Planet. Sci.* **43**, 261–272.

Associate editor: Christian Koeberl